JOURNAL OF PROPULSION AND POWER
Vol. 23, No. 2, March–April 2007

Vortex Structure Produced by a Laterally Inclined Supersonic Jet in Transonic Crossflow

Steven J. Beresh,* John F. Henfling,† Rocky J. Erven,‡ and Russell W. Spillers§
Sandia National Laboratories, Albuquerque, New Mexico 87185

DOI: 10.2514/1.25444

Stereoscopic particle image velocimetry data have been collected for a supersonic jet exhausting into a transonic crossflow from a laterally inclined scarfed nozzle installed flush in a flat plate. Mean velocity fields and their derived vorticity were measured at a single crossplane in the far-field for varied jet-to-freestream dynamic pressure ratio J and nozzle inclination angles of 0, 15, 30, and 45 deg. The data reveal the induced counterrotating vortex pair and the horseshoe vortex formed as the jet exits the nozzle, both of which appear symmetric for the uncanted nozzle. As the nozzle inclination is increased, the vortex pair becomes tilted opposite the nozzle cant and shifts closer to the wall, where the lower vortex attains a larger strength than its counterpart until it eventually becomes so dominant that the opposite vortex is undetectable. Regardless of nozzle cant, vortex strengths increase with larger J. Vortex distances from the wall increase with J at lower nozzle cants, but at larger inclination, the position of the vortex nearer the wall varies less with J than does its complement. Thus, at a sufficiently large nozzle cant, the jet interaction effectively produces a single vortex whose position does not shift greatly with jet strength.

Introduction

ATMOSPHERIC flight vehicles that employ supersonic jets for attitude or roll control may find their expected performance degraded as the emerging jet turns over and travels downstream where it can interfere with control surfaces such as fins or strakes. Past studies have indicated that this jet/fin interaction can change the pressure field on the fins and hence the force they generate [1–6]. This interaction is fundamentally the result of an interaction occurring upstream between the exhausting jet and the crossflowing freestream, because it establishes the flowfield structure that subsequently impinges upon the fins. The far-field of the jet-in-crossflow interaction is dominated by the presence of a counterrotating vortex pair (CVP), shown in the sketch in Fig. 1, which is induced as the jet is realigned by its encounter with the freestream. Knowledge of this vortex pair is largely extrapolated from low-speed studies in which measurements are more easily made (for example, [7–9]), but these vortices have been directly detected in supersonic flowfields as well [10,11]. Additionally present are horseshoe vortices (HSV) formed when they wrap around the obstruction presented by the jet as it first exits from the nozzle [8,12,13], as well as the unsteady wake vortices analogous to the vortex street found in the wake of a cylinder [8,9]. This strong vortex system is believed to be principally responsible for the interaction with downstream fins.

Whereas past studies associated with the present work have examined the vortices produced by an axisymmetric nozzle exhausting normally into a transonic crossflow [14–16], geometric constraints commonly require flight vehicles to use nozzles inclined with respect to the surface from which they exhaust. In addition to altering the thrust vector, the resulting asymmetry creates a scarfed nozzle, wherein the conical contour is truncated by the vehicle surface to produce a nonuniform nozzle expansion length. The exiting jet, therefore, will be asymmetric, as will the vortices induced by the interaction, and this alteration in the vortex structure can be expected to have implications for a downstream interaction with the fins or other control surfaces.

The present study experimentally examines the vortex structure generated by a supersonic jet exhausting from a scarfed, inclined nozzle flush with a flat plate into a transonic crossflow. Vortices are identified from planar velocity fields measured using stereoscopic particle image velocimetry (PIV) in the crossplane of the far-field of the jet interaction. Although inclined jets in crossflow have been the subject of past experimental investigations, most have been incompressible whose intended applications are flow control, film cooling, or mixing enhancement [17–22]. High-speed studies have included inclined sonic jets [23–25] as well as scarfed supersonic nozzles [26] angularly injected into a supersonic freestream. None of these compressible studies (excepting the yawed cases in a portion of [25]), however, employed a jet inclined perpendicularly to the freestream; rather, the jet was angled within the streamwise plane as a means of enhancing mixing for scramjet development. In the current study, the jet exhausts within the plane normal to the freestream direction, as would a control jet oriented in the lateral direction on a flight vehicle. In this regard, the present work appears unique in its examination of the induced vortices from laterally inclined scarfed supersonic nozzles in transonic crossflow and its ramifications for aerodynamic control.

Experimental Apparatus

Trisonic Wind Tunnel

Experiments were performed in Sandia's Trisonic Wind Tunnel (TWT), which is a blowdown-to-atmosphere facility using air as the test gas through a 305×305 mm^2 (12×12 in^2) rectangular test section enclosed within a pressurized plenum. The solid-wall transonic test section was used rather than the traditional porous walls, which served both to supply a flat plate from which the jet will issue and to provide computationally tractable boundary conditions for comparison of experimental data and numerical simulations. The use of a solid-wall test section limits the Mach number range of the flowfield, but this was considered an acceptable compromise.

Supersonic Jet Hardware

Four jet nozzles were tested, one oriented normal with respect to the flat plate from which it exhausts and three having inclination angles of 15, 30, and 45 deg with respect to the wall normal. The

---

Presented as Paper 4653 at the 35th AIAA Fluid Dynamics Conference, Toronto, Ontario, Canada, 6–9 June 2005; received 25 May 2006; accepted for publication 18 July 2006.

*Principal Member of the Technical Staff, Engineering Sciences Center, P. O. Box 5800, Mail Stop 0834; sjberes@sandia.gov. Senior Member AIAA.

†Distinguished Technologist. Member AIAA.

‡Principal Technologist.

§Technologist.

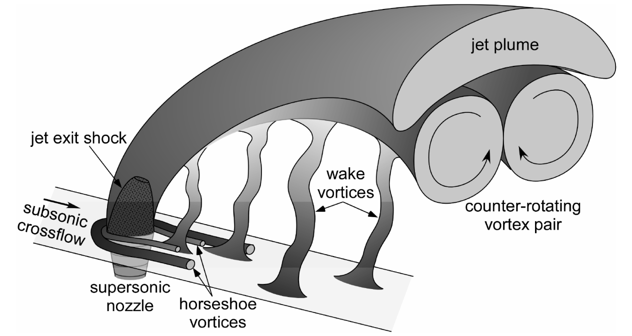

Fig. 1 Features common to a symmetric jet-in-crossflow interaction.

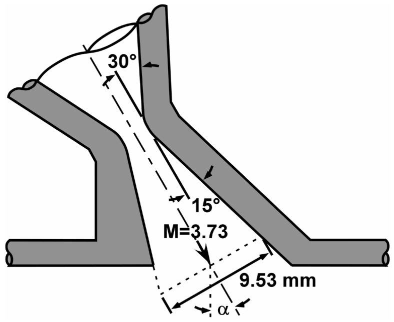

Fig. 2 Supersonic nozzle inclined to the flat plate from which it exhausts.

normal jet employs a conical nozzle with an expansion half-angle of 15 deg and an exit diameter of 9.53 mm (0.375 in.). The three inclined nozzles are designed such that when tipped to the flat plate, the original conical nozzle is scarfed by the plate through the centerpoint of the normal exit plane, as shown in Fig. 2 (not to scale). Therefore, the centerline Mach number matches for all four nozzles, but the inclined nozzles possess an expansion shorter than the normal nozzle for one-half its exit and longer for the other half. The variation of the nozzle exit Mach number due to the cant angle α (which is identical to the scarf angle for the present nozzle design) is enumerated in Table 1. Also given are the minor and major axis lengths of the ellipse forming the exit plane; note that the center of this ellipse is not located on the nozzle centerline when $\alpha \neq 0$ deg. For all nozzles, regardless of the scarf angle, the short edge retains an exit Mach number sufficiently large to ensure that waves emanating from the nozzle exit do not propagate within the nozzle itself. Therefore, quasi-one-dimensional nozzle gas dynamics can be expected to hold [27], except at low nozzle pressures where asymmetric internal flow separation is likely [28].

The nozzle was mounted along the centerline of the top wall of the test section, which served as the flat plate from which it transversely exhausts. Each nozzle insert has a circular shape to allow its installation at any angle with respect to the wind tunnel freestream, although in the present study the nozzles were mounted exclusively perpendicular to the freestream (i.e., the nozzle cant remains within the crossplane). Each nozzle fit to a settling chamber designed for a maximum pressure of 14 MPa (2000 psia) and instrumented to provide stagnation pressure and temperature measurements. Nitrogen was used as the working gas for the jet.

Table 1 Nozzle exit properties due to the nozzle inclination

α	M_{short}	M_{center}	M_{long}	d_{minor}	d_{major}
0 deg	3.73	3.73	3.73	9.53 mm	9.53 mm
15 deg	3.57	3.73	3.88	9.55 mm	9.91 mm
30 deg	3.41	3.73	4.09	9.64 mm	11.27 mm
45 deg	3.21	3.73	4.42	9.89 mm	14.51 mm

A sidewall window flush with the top wall was positioned downstream of the jet for viewing the far-field of the interaction; a larger window in the pressurized plenum complemented the test section window. A window in the floor of the test section was located near the position of the sidewall window for introducing the laser sheet, which was matched by a second laser window in the bottom of the plenum. The relative position of the jet and windows within the test section is sketched in Fig. 3 (not to scale), which additionally shows the laser sheet for the crossplane PIV measurements and sidewall pressure taps for measuring the test section static pressure used to determine the freestream Mach number.

Particle Image Velocimetry System

PIV measurements were acquired with the laser sheet normal to the wind tunnel axis, as shown in Fig. 3, and aligned to the midpoint of the sidewall window 321.8 mm downstream of the jet nozzle centerline. This position corresponds to 33.8 jet diameters d_j downstream, where d_j is found from the normal nozzle exit plane. The laser sheet was angled within the wind tunnel crossplane such that it projected asymmetrically across the test section, illuminating an imaging region prejudiced toward the side where the inclined jet nozzles were directed. The coordinate system is chosen such that the u component lies in the streamwise direction and the v component is in the vertical direction, positive away from the top wall; the w component is chosen for a right-handed coordinate system. The origin is located at the centerpoint of the normal jet nozzle exit plane.

The light source was a pair of frequency-doubled Nd:YAG lasers (Coherent Infinity 40-100) that produced about 120 mJ per beam. The beams were combined and formed into coplanar sheets, then directed into the test section. The crossplane PIV configuration aligns the freestream direction of the wind tunnel with the out-of-plane motion through the laser sheet; therefore, to limit the resulting particle dropout, a thick laser sheet of 2.0 mm and a short time between pulses of 1.80 μs were employed.

The TWT is seeded by a thermal smoke generator (Corona Vi-Count 5000) that produces a large quantity of particles typically 0.2–0.3 μm in diameter from a mineral oil base. Particles are delivered to the TWT's stagnation chamber upstream of the flow conditioning section while the jet itself remains unseeded. Although this creates a serious measurement bias near the jet exit due to selective flow sampling, data acquired further downstream are not subject to such a difficulty because turbulent mixing entrains particles from the freestream and distributes them throughout the interaction once in the far-field. The particles are sufficiently small that they rapidly attain the local velocity once they have been redistributed [29,30].

Scattered laser light was collected by frame-straddling charge-coupled device cameras (Redlake MegaPlus ES4.0/E) with a resolution of 2048 × 2048 pixels digitized at 8 bits and operated at five image pairs per second. The cameras were equipped with 105 mm lenses (Nikon Micro-Nikkor) mounted on Scheimpflug platforms for an oblique focal plane. Both cameras looked through the same test section window, viewing the laser sheet from opposite directions, because placing one camera at the other sidewall window precludes access to the test section. To improve upon the limited camera viewing angles due to the constricted optical access, mirrors were rigidly mounted inside the plenum to reflect scattered laser light to the cameras at a sharper angle, which allowed an angle of 53 deg between the camera lenses and the laser sheet normal. The limited optical access additionally prevents meaningful movement of the imaging location upstream or downstream; thus all data have been acquired at a single position.

The stereoscopic system has been calibrated using the distorted sheet procedure described by Soloff et al. [31], alternatively known as a "thick sheet" or multiplane calibration. An aluminum plate 3.05 mm (0.120 in.) thick and flat to within 0.05 mm (0.002 in.) was fabricated with holes drilled every 12.7 mm (0.500 in.) as fiduciary marks. Both surfaces of the plate had been sandblasted to create

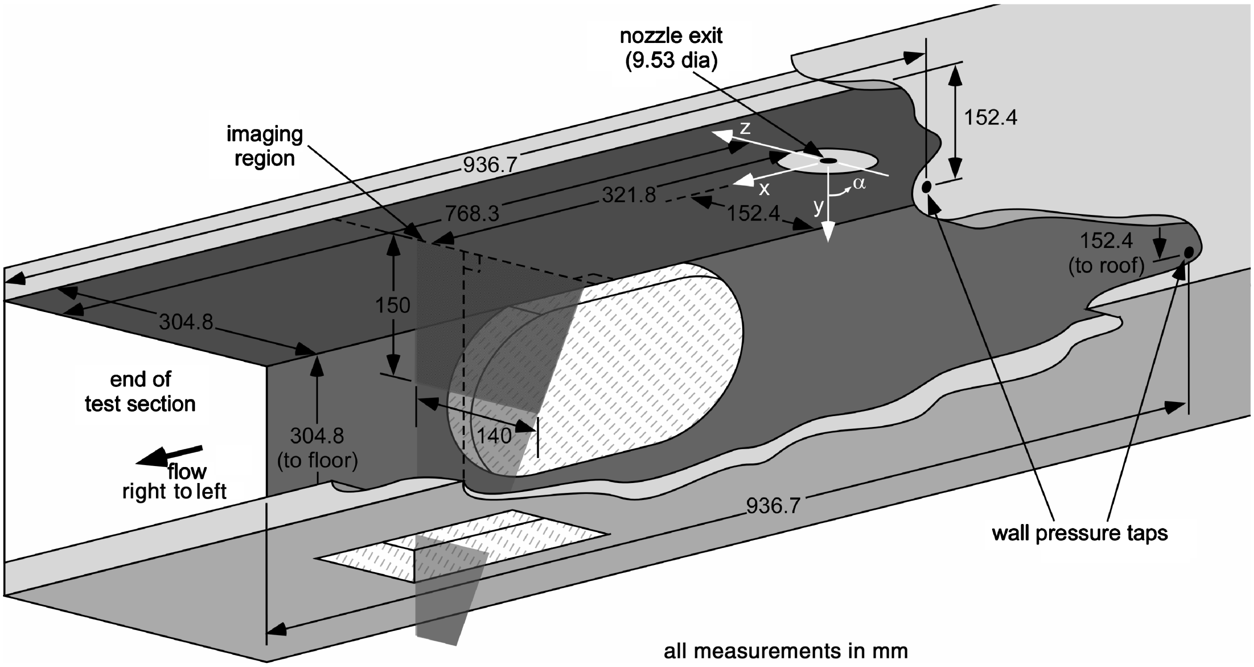

Fig. 3 Schematic of the experimental configuration, looking downstream from beneath the wind tunnel.

speckle patterns upon which the PIV software could correlate. Green LED lamps were used for illumination to produce sharper speckle patterns than those from white light, as well as providing a narrow wavelength nearly matching that of the laser to assure no refocusing due to chromatic aberration. The calibration target was precisely aligned normal to the test section axis and translated through the thickness of the measurement volume while a sequence of images was acquired by each camera. The resulting calibration images were used by the data processing software (IDT's Provision 2.02) to tie together the two sets of image pairs to produce three-dimensional vectors.

Sequences of 150 image pairs from each camera were acquired in a single wind tunnel run for each set of flow conditions. Images were interrogated with a 64×64 pixel window employing adaptive correlations and a spatial offset to account for the streamwise particle displacement. The spatial resolution varies across the image due to the oblique camera view; at the wind tunnel centerline, it is 9.8 mm horizontally and 6.0 mm vertically. An approximate 50% overlap in adjacent interrogation windows was typically used to oversample the velocity fields. The resulting vector fields were validated based upon signal-to-noise ratio and nearest-neighbor comparisons.

Experimental Conditions

The freestream Mach number is $M_\infty = 0.8$ with a wind tunnel stagnation pressure $P_0 = 154$ kPa (22.4 psia), which yields a test section static pressure $p_w = 101$ kPa (14.7 psia). The wind tunnel Reynolds number at these conditions is 20×10^6 m^{-1} (6×10^6 ft^{-1}). The nominal stagnation pressure for the jet is $P_{0j} = 4.96$ MPa (720 psia), providing a centerline jet exit pressure of $p_e = 47.1$ kPa (6.84 psia) on the nozzle centerline. These conditions combine to produce a nominal jet-to-freestream dynamic pressure ratio $J = 10.2$ (in the present work, J is defined on the nozzle centerline). Additional cases span a range of J values while maintaining $M_\infty = 0.8$, but P_{0j} was always chosen such that the jet was overexpanded. The wall pressure p_w was measured from the mean of two static pressure taps located on the wind tunnel side walls 168 mm upstream of the jet nozzle centerline, as seen in Fig. 3. M_∞ and the velocity reference U_∞ were calculated isentropically from the ratio p_w/P_0 and the stagnation temperature T_0.

The gas supply for the jet was unheated, so the jet stagnation temperature T_{0j} varied from 297 to 309 K (534–556 R) depending upon the laboratory ambient conditions. The wind tunnel air supply is heated in the storage tanks, but not temperature-controlled subsequent to this; therefore, the freestream stagnation temperature T_0 also is subject to slight variation and fluctuated from 321 to 331 K (577–596 R).

The 99% velocity boundary layer thickness has been measured as 14.8 ± 0.4 mm (0.58 ± 0.02 in.) from PIV data acquired in the streamwise plane [14]. This measurement was acquired on the wind tunnel centerline 254 mm downstream of the usual centerpoint of the jet nozzle exit, though the nozzle had been replaced by a blank for these measurements.

Results and Discussion

Velocity Fields

Mean velocity data are shown in Fig. 4 for all five values of J for the normal jet nozzle (i.e., $\alpha = 0$ deg). In-plane velocities are displayed as vectors superposed upon a contour plot of the out-of-plane (streamwise) velocities. The axes have been normalized to d_j and velocities are normalized to the freestream velocity U_∞. In-plane velocity bias errors stemming from the stereoscopic camera calibration have been corrected using undisturbed freestream data as described in [16], where the lateral motion is known to be nearly zero as determined by wind tunnel flow angularity studies, and hence can be assumed to result principally from measurement bias. Out-of-plane velocity biases remain uncorrected primarily because this component of the error unidentifiably varies with J and hence cannot be corrected using jet-off measurements.

The vector fields in Fig. 4 clearly show the CVP induced by the jet-in-crossflow interaction, which is centered near the lower portion of the streamwise velocity deficit given by the contours. This is consistent with two-dimensional PIV data acquired along the wind tunnel centerline, which showed the vortex pair to be situated below the decaying jet [14]. It also is evident that a narrow wake exists along the centerline, where the streamwise velocity has not fully recovered; this, too, was observed in the two-dimensional PIV [14]. Finally, strong streamwise velocity deficits near the wall within the boundary layer indicate the remnant of the HSV that forms around the jet plume immediately after exit from the nozzle. Vortical motion is visible in

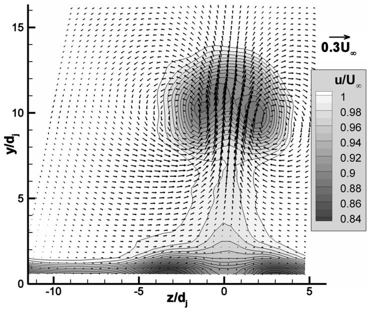

a) J=16.7

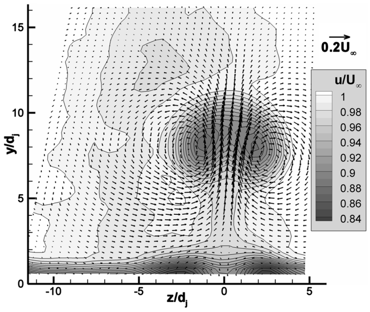

b) J=10.2

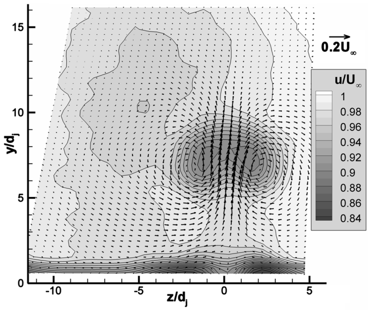

c) J=8.1

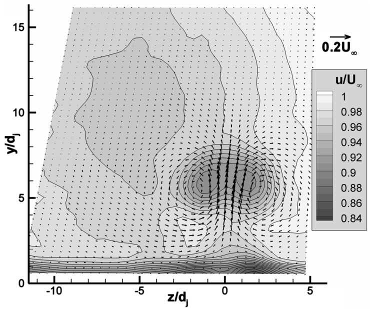

d) J=5.6

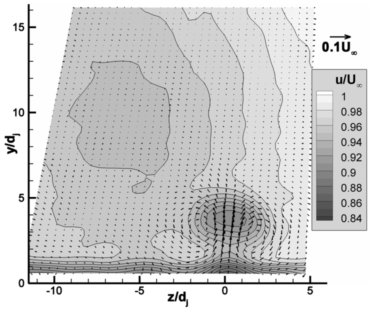

e) J=2.8

Fig. 4 Mean velocity data for the uncanted nozzle ($\alpha = 0\,\mathrm{deg}$).

the HSV velocity vectors for the two larger J values, but clearly possesses an appreciably smaller magnitude than that associated with the CVP. Both the CVP and the HSV are visually symmetric to match the symmetry of this nozzle geometry.

The five cases of Fig. 4 show how the flowfield changes with the strength of the jet. It is evident that the size of the jet and the CVP as well as their distance from the wall increase as J becomes larger, consistent with the earlier streamwise measurements [14]. Larger J induces stronger in-plane velocities associated with the CVP. Furthermore, the streamwise velocity deficit induced by the jet can be seen to increase slightly for greater J while its size expands markedly. A similar trend is evident in the horseshoe vortices. The HSV appears to combine into one structure for $J = 2.8$, which is consistent with the trend of narrowing distance between these two vortices as J is lowered, but this instead may result from limits in the spatial resolution. Further discussion of the flowfield produced by the uncanted nozzle can be found in [16]; the present measurements were found to lie within the measurement uncertainty of those in [16].

It is readily apparent in Fig. 4 that as J is reduced, an unexplained velocity deficit appears in the streamwise component concentrated toward the $-z$ side of the CVP. This is an artifact of the PIV calibration error that could not be corrected in the streamwise direction as it was for the in-plane components. Despite its variation with J, it has been shown to arise from measurement error as opposed to a physical effect because different camera positions (and calibrations) return different errors. The reduction of this error at higher J is not due to saturation of the contour plots. No explanation has been determined for its dependence upon J.

The velocity fields for the three scarfed nozzles are shown in Figs. 5–7 for $\alpha = 15$, 30, and 45 deg, respectively. Even for the mildest cant angle of $\alpha = 15$ deg in Fig. 5, differences in the vortex structure are readily visible, but they are not identical for all values of J. In Figs. 5b–5d, in which the midrange values of J are shown, the CVP seen in the normal nozzle case of Fig. 4 now essentially appears tilted, although it is canted opposite the direction that would keep it aligned with the inclined nozzle axis. As this happens, the upper, leftward vortex in the CVP (which is of negative vorticity, because the positive x axis is into the page) induces a larger streamwise velocity deficit than its counterpart. (As described later, however, this does not necessarily indicate that the vortex itself is stronger.) Similarly, the leftward vortex in the HSV creates a streamwise velocity deficit greater in both magnitude and extent as compared with its complement, which is nearly invisible for every case, possibly because it is too small and near the wall to detect. The vortex structure for the $J = 16.7$ case is somewhat different, as the CVP is much more strongly dominated by the negative vortex; the positive vortex induces only a small streamwise velocity deficit and appears to have bifurcated into two vortices stacked upon each other, as evident by the in-plane velocity vectors. In contrast, at $J = 2.8$, the negative vortex of the CVP has virtually disappeared and only the positive vortex has an appreciable presence.

These trends continue in Fig. 6 for $\alpha = 30$ deg. Figures 6a–6c , for the largest values of J, show a CVP tipped further away from alignment with the wall, although now the strongest streamwise velocity deficit is found for the lower, rightward vortex (of positive vorticity) in the CVP, in contrast to the $\alpha = 15$ deg case. As in the previous cant angle, only one vortex in the HSV is detectable. The $J = 16.7$ case no longer displays a bifurcated positive vortex. The $J = 2.8$ case is nearly indistinguishable from its $\alpha = 15$ deg behavior, in which only the positive vortex in the CVP is visible, and the $J = 5.6$ case now bears similarity to it in that it also shows only a single significant vortex.

Figure 7 shows that for $\alpha = 45$ deg, all five values of J produce velocity fields in which only one vortex of the CVP is dominant. For the two largest values of J, in Figs. 7a and 7b, the presence of the negative vortex is notable principally as an extension to the shape of the streamwise velocity deficit and is not obvious through the in-plane velocity vectors; one vortex of the HSV is weakly detectable in the streamwise component. The remainder of the J cases essentially display flow structure composed of but a single vortex. Over the

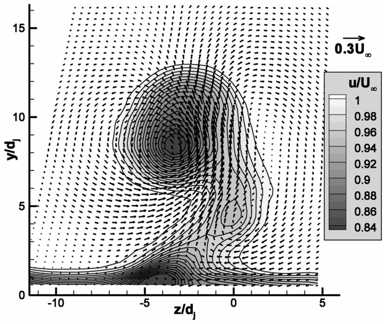

a) J=16.7

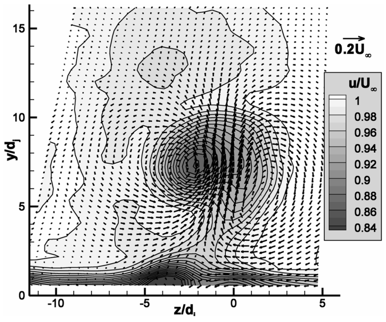

b) J=10.2

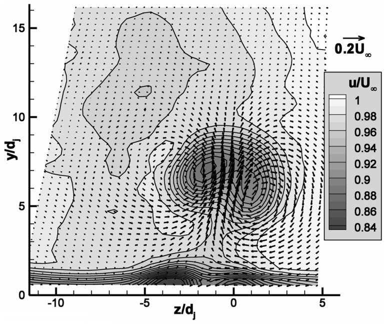

c) J=8.1

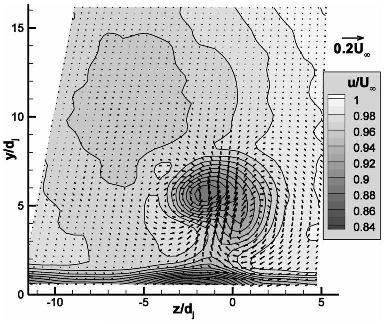

d) J=5.6

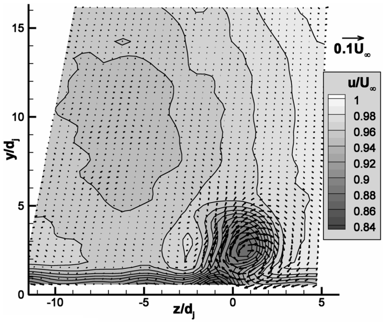

e) J= 2.8

Fig. 5 Mean velocity data for the nozzle canted at $\alpha = 15$ deg.

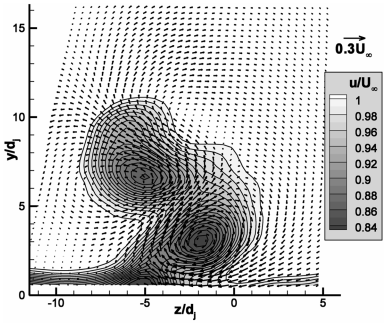

a) J=16.7

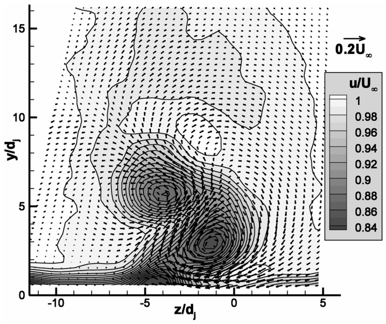

b) J=10.2

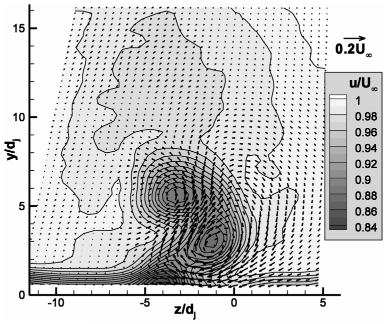

c) J=8.1

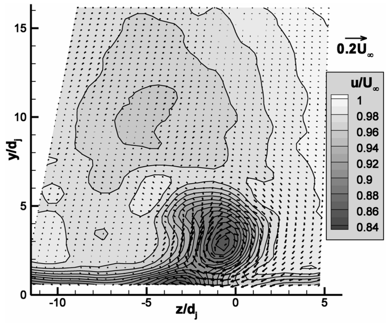

d) J=5.6

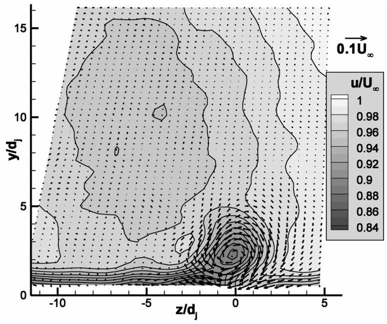

e) J=2.8

Fig. 6 Mean velocity data for the nozzle canted at $\alpha = 30$ deg.

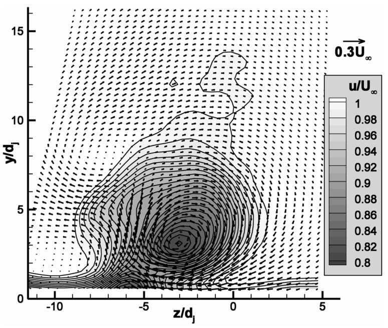

a) J=16.7

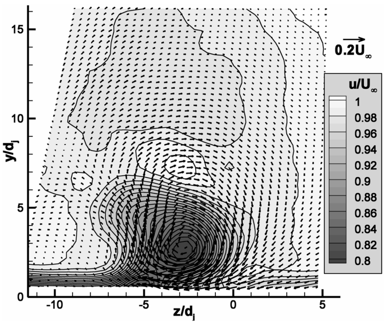

b) J=10.2

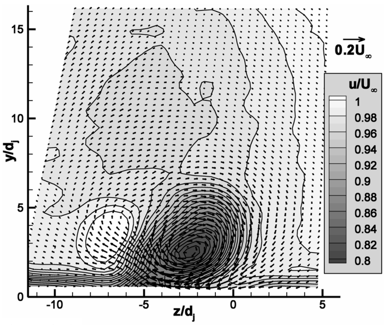

c) J=8.1

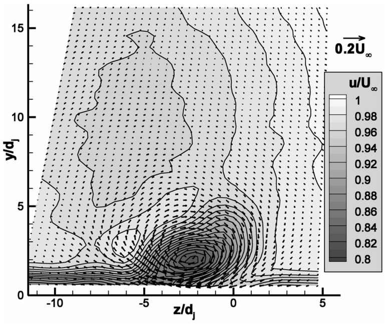

d) J=5.6

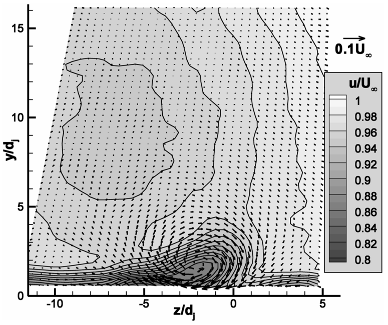

e) J=2.8

Fig. 7 Mean velocity data for the nozzle canted at $\alpha = 45\,\mathrm{deg}$.

entire range of J, the magnitude of the streamwise velocity deficit is greater than in the previous nozzle inclinations (note the contour scale has been altered in comparison with Figs. 4–6).

Vorticity Fields

The vorticity in the x direction is easily calculated from the in-plane component of the mean velocity fields of Figs. 4–7 using a finite-difference scheme and is shown in Figs. 8–11 for $\alpha = 0, 15, 30$, and 45 deg, respectively, normalized by d_j and U_∞. Note that the positive vorticity axis is into the page, as this is the direction of the positive x axis. Greater precision error can be expected in the vorticity fields than in the mean velocity fields because smaller errors in velocity become magnified in a derived quantity [32]; this is particularly true for the present data set in which the mean measurements are determined from a relatively small set of instantaneous realizations. On the other hand, the effects of the PIV calibration bias errors are smaller than in the velocity fields because they are characterized by low spatial frequency across the field and hence do not appreciably contribute to the derivatives used to compute the vorticity. Figures 8–11 clearly depict the CVP, but the HSV is, at best, only weakly detected; this is expected given the velocity fields from which they are computed, as the in-plane vectors do not show the presence of the HSV as strongly as the steamwise velocity deficit. The apparent mild degree of asymmetry between the two vortices of the CVP in the $\alpha = 0$ deg data shown in Fig. 8 lies within the uncertainty, although more precise related work has shown that the CVP is in fact mildly asymmetric despite the nominally symmetric flowfield [16].

The size, strength, and location of the CVP are more directly observed through their vorticity fields than were possible from the velocity data. Figure 8 shows that for $\alpha = 0$ deg, the CVP grows larger and stronger, as well as more distant from the wall, as J is increased. In Fig. 9, where $\alpha = 15$ deg, the tilt to the CVP alignment with respect to the wall is as evident in the vorticity fields as it was in the streamwise velocity deficit shown in Fig. 5. The bifurcated positive vortex at $J = 16.7$ is clear in Fig. 9a and, additionally, the positive vortex at $J = 10.2$ displays a significant vertical stretching as well, as if it were in a precursor stage to bifurcation; this behavior at $J = 10.2$ was not obvious in the velocity field in Fig. 5b. Figure 9 also shows that it is not indisputable that the negative vortex is stronger at $J = 8.1$ and $J = 5.6$, which appeared to be the case from the streamwise velocity deficits. Regardless of these behavioral variations, the vorticity magnitude and the CVP distance from the wall are greater for larger values of J.

The vorticity behavior at $\alpha = 30$ deg, in Fig. 10, is more consistent across all values of J. In all cases, the positive vortex possesses a greater magnitude than does the negative vortex, and these magnitudes are greater for larger J. Some amount of vortex stretching and bifurcation of the positive vortex is visible at $J = 16.7$ and 10.2, although unlike at $\alpha = 15$ deg, here the principal strength of the vortex remains concentrated nearer the wall. The CVP is tilted further as compared with the $\alpha = 15$ deg case, and is located further from the wall for increased J, although not as far from the wall as for $\alpha = 15$ deg. These trends continue for the $\alpha = 45$ deg case in Fig. 11, where the positive vortex thoroughly dominates the negative vortex, the latter of which is not even detectable at $J = 5.6$ and $J = 2.8$. The CVP, if it still can be considered a vortex pair, resides closest to the wall of all the nozzle inclinations, as was previously apparent in the velocity fields of Fig. 7.

The observation that, at the largest nozzle cant, the positive vortex dominates the flowfield structure is consistent with incompressible studies in which only one strong vortex could be detected in the far-field for laterally inclined jets of comparable J [18,22]. The asymmetric nature of the vortex pair produced by any of the inclined jets is due, at least in part, to the nonuniform Mach number across the scarfed nozzle, but an additional factor may be the variation in the nozzle boundary layer thickness around the circumference of the nozzle wall, given that the formation of the CVP is believed to be initiated by the vorticity emanating from the jet nozzle [9,33–36].

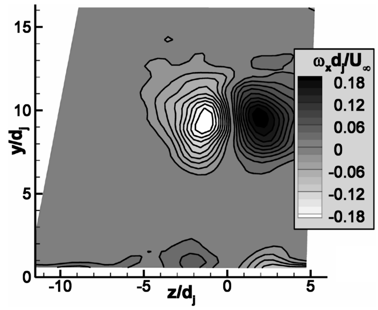

a) J=16.7

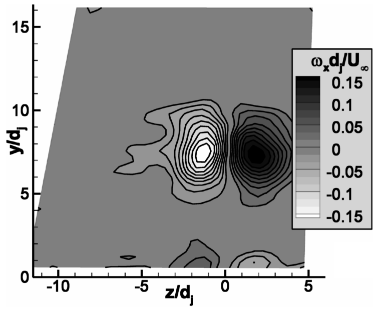

b) J=10.2

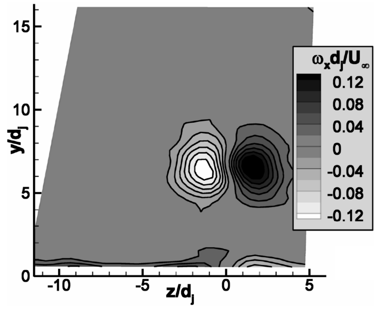

c) J=8.1

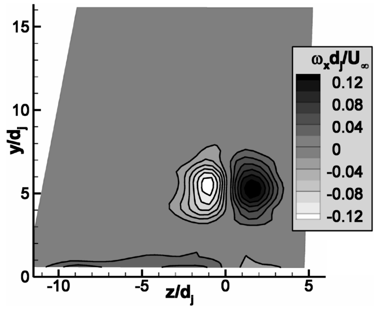

d) J=5.6

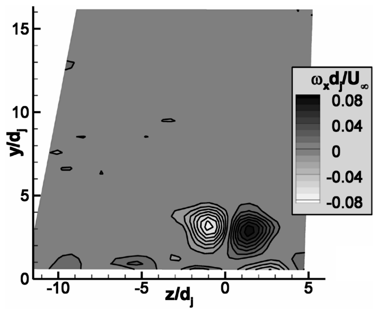

e) J=2.8

Fig. 8 Vorticity fields derived from the in-plane velocity data of Fig. 4 for $\alpha = 0\,\text{deg}$.

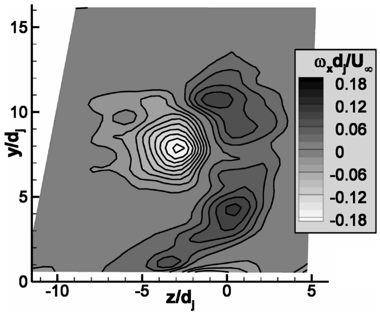

a) J=16.7

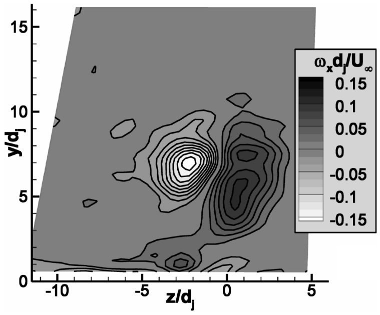

b) J=10.2

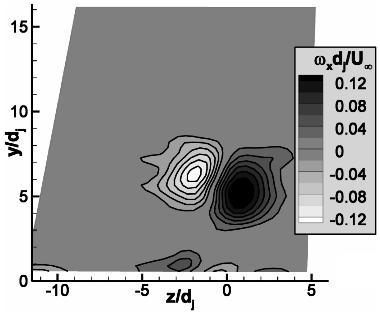

c) J=8.1

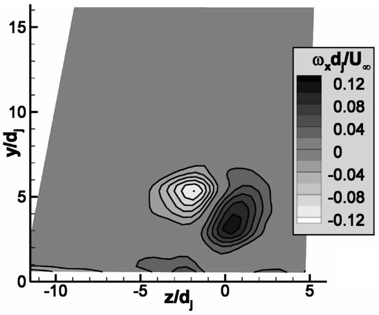

d) J=5.6

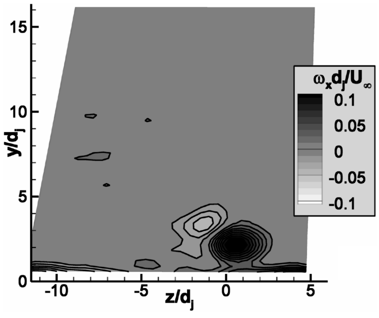

e) J=2.8

Fig. 9 Vorticity fields derived from the in-plane velocity data of Fig. 5 for $\alpha = 15\,\text{deg}$.

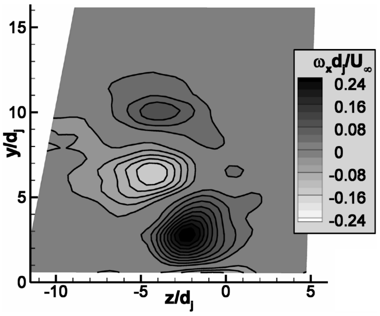

a) J=16.7

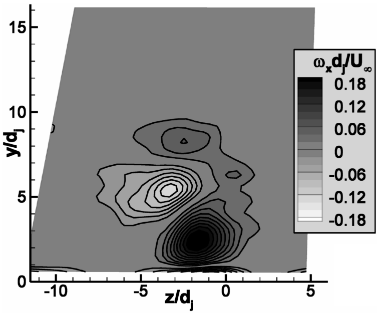

b) J=10.2

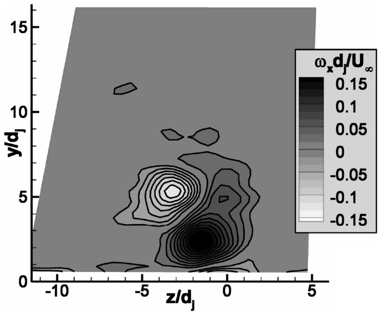

c) J=8.1

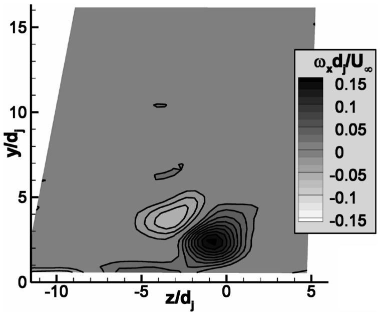

d) J=5.6

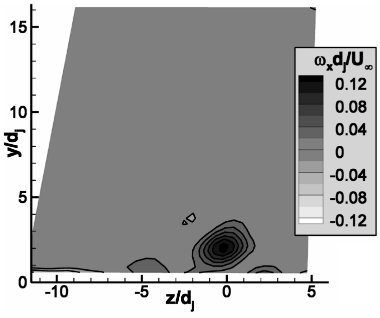

e) J=2.8

Fig. 10 Vorticity fields derived from the in-plane velocity data of Fig. 6 for $\alpha = 30$ deg.

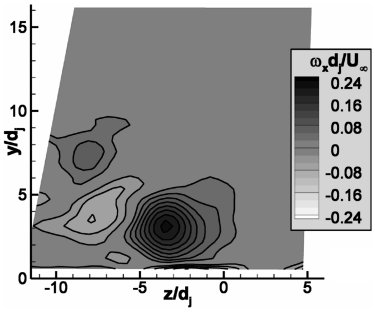

a) J=16.7

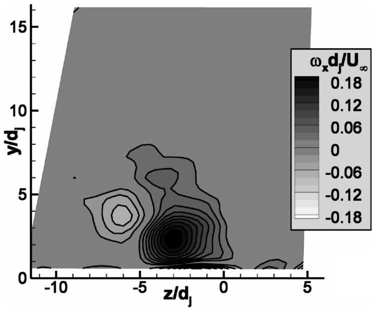

b) J=10.2

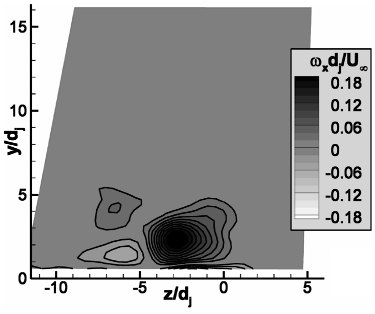

c) J=8.1

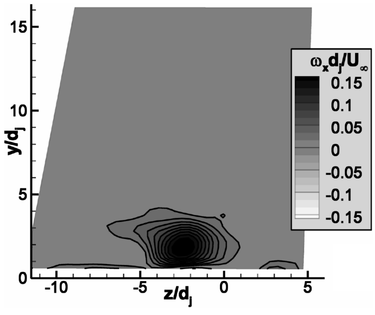

d) J=5.6

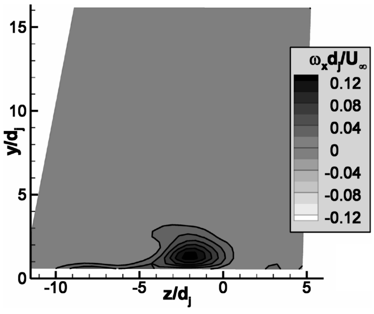

e) J=2.8

Fig. 11 Vorticity fields derived from the in-plane velocity data of Fig. 7 for $\alpha = 45$ deg.

Uncertainty Analysis

The uncertainty of the mean velocity measurements is separable into a precision error, consisting of PIV correlation error, measurement repeatability, and data convergence error; and a bias error arising principally from the PIV camera calibration. The precision error is assessed straightforwardly using multiple wind tunnel runs for the $J = 10.2$ and $\alpha = 0$ deg case, from which the uncertainty was found as the 95% confidence interval of the scatter in the measurements. These results include the effect of variations in J and M_∞ between wind tunnel runs, which typically are ± 0.2 and ± 0.003, respectively. The calibration bias was found by reinstating the calibration target into the measurement location and traversing it a known distance in two dimensions corresponding to the expected particle motion in the time between laser pulses, then processing the resulting images as if they were PIV data. Bias values were found from the deviation of the measured translation with the actual motion. Though the in-plane components of the calibration bias have been corrected using the freestream measurements, it is unclear to what extent this reduces the uncertainty; therefore it is conservative to estimate the total uncertainty including the calibration bias. Combining all enumerated error sources, uncertainties were calculated as ± 10, ± 6, and ± 8 m/s in the u, v, and w components, respectively, which equate to 0.035, 0.02, and $0.03U_\infty$, respectively.

The uncertainty in the vorticity can be found by propagating the uncertainties determined for the velocity measurements. However, the influence of the precision component of the velocity uncertainty upon the vorticity dominates that of the velocity bias because the camera calibration biases are of low spatial frequency; therefore, when the vorticity is calculated, the biases largely cancel out through the derivative computation. This approach yields a vorticity uncertainty estimate of ± 0.025 in terms of $\omega_x d_j/U_\infty$. Nearly the same estimate is found by instead examining the deviation of several repeated wind tunnel runs for the same flow conditions.

In an ideal flowfield, the same vortex structure would be produced regardless of whether the inclined nozzle faces the $+z$ direction or the $-z$ direction. However, every wind tunnel has some degree of flow nonuniformity, which may influence the development of the CVP and its downstream evolution. This was tested in the present experiment by installing the $\alpha = 30$ deg nozzle facing $+z$ rather than the $-z$ orientation used for most of the study, and then repeating a few cases. Although the off-centerline position of the imaging region prevented visualization of the entire vortex structure, a sufficient portion could be observed to compare with the standard measurements. The results indicated that a small number of velocity comparisons between the standard and inverted cases exceeded the data uncertainty by a slight degree, but most disparities could not be considered significant. Deviation was more likely at large values of J. Nevertheless, in all cases the qualitative structure of the flow and the strength and location of the vortices were found in close agreement.

It is conceivable that the vortex structure of the interaction is influenced by the presence of the wind tunnel walls, particularly at large values of J. Unfortunately, it is not straightforward to experimentally quantify this potential error source due to hardware limitations concerning relocation of the jet nozzle, and additionally noting that an alteration of the nozzle size would influence the interaction through a change in its relationship to the boundary layer thickness. If wall interference is an issue, it is probable that the flow structure would be impacted at large values of J as compared with smaller J. The flow structure at $J = 16.7$ (and, to a lesser extent, at $J = 10.2$) does differ from the lower-J cases in that the positive vortex appears diffuse and bifurcated, but it is noteworthy that this effect occurs in the vortex that is farther from the wind tunnel side walls. Furthermore, similar behavior was observed for large J in a jet-in-crossflow interaction on a full-scale flight vehicle, in which the scale of the jet relative to the wind tunnel was much less than in the present case [37]. Therefore, it is not certain that this effect at higher values of J is related to confinement within the wind tunnel.

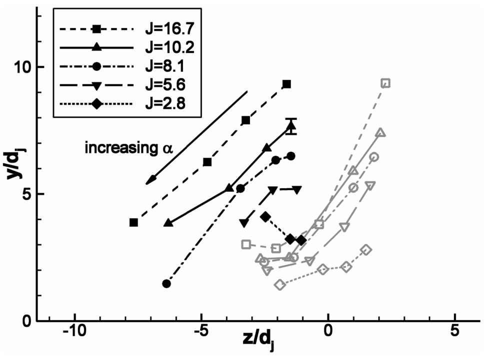

Fig. 12 Vortex positions as defined by the vorticity centroids.

Vortex Characteristics

The vorticity fields of Figs. 8–11 are ideally suited to tracking the variation in the CVP position and strength as both J and α are altered. These values were determined by employing an integration of the vorticity magnitude for each vortex in the CVP. The integrated vorticity Γ_x (i.e., the circulation) was computed as per

$$\Gamma_x = \int \omega_x \, \mathrm{d}A \tag{1}$$

by numerically integrating the measured vorticity field over an area whose perimeter was defined by first locating the locus of values 37% $(1/e)$ of the maximum vorticity for that particular case, then extending the perimeter until the slope at each point intersected zero vorticity to better capture the entirety of the vortex. This threshold is somewhat arbitrary in that it was selected not for any physical reason, but because it was found to consistently produce a sensible definition of the vortices; lower thresholds tended to incorporate noise from the vorticity field, especially at lower values of J. The centroid of the vortex was found over the same perimeter by

$$(\bar{y}, \bar{z}) = \frac{1}{\Gamma_x} \int (y, z)\omega_x \, \mathrm{d}A \tag{2}$$

Results using these definitions were found to be in reasonable agreement with simply tracking the magnitude and positions of the peak vorticity magnitudes, which tends to validate the utility of the perimeter as defined herein.

The resulting vortex locations are given in Fig. 12 for the positive and negative vortices for all five values of J, tracing trajectories as α is altered over its range. Negative vortices are shown by dark lines and positive vortices by grey lines. The negative vortex was not located for the $\alpha = 45$ deg case at $J = 5.6$ and $J = 2.8$ because, as Fig. 11 shows, it was not detectable. Error estimates were derived from the variations between multiple wind tunnel runs for the $J = 10.2$ and $\alpha = 0$ deg case. The plot shows that the negative vortex moves toward the wall and in the $-z$ direction as α is increased, that is, in the direction of nozzle inclination. The positive vortex behaves similarly, but does so in a more nonlinear fashion. Interestingly, as α is increased, the position of the positive vortex varies less with J than does the negative vortex; this observation is consistent with the behavior of a jet-in-crossflow from a highly-scarfed nozzle on a flight vehicle configuration [37].

Figure 13 shows the circulation on separate plots for the negative and positive vortices. Uncertainty estimates again were derived from repeated wind tunnel runs at $J = 10.2$ and $\alpha = 0$ deg. Regardless of the vorticity sign, a larger value of J produces a stronger vortex, as anticipated. The negative vortex displays a generally diminishing vortex strength as α increases. For the positive vortex, the strength is slightly increasing as α increases (with an obvious discordant data point for $J = 16.7$ at $\alpha = 15$ deg where the vortex appeared to bifurcate), though this trend is difficult to consider significant in

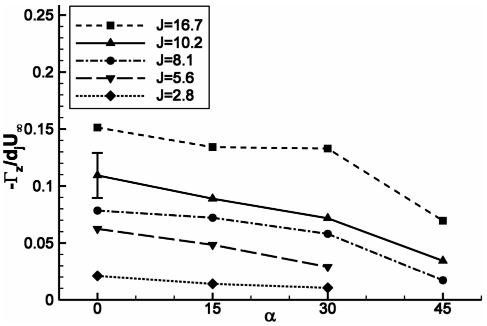

a) negative vortices

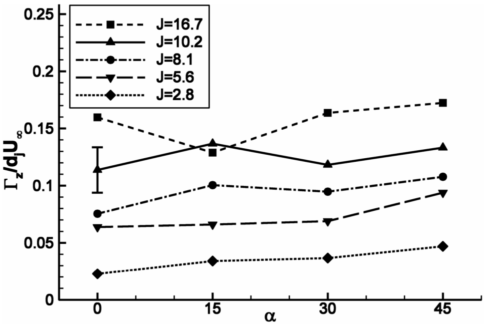

b) positive vortices

Fig. 13 Vortex strengths as defined by the circulation.

comparison to the uncertainty estimate. These trends indicate that in nearly all cases for the three inclined nozzles, the positive vortex possesses a greater vortex strength than does the negative vortex; this is true even at $\alpha = 15$ deg where the streamwise velocity deficit was actually greater for the negative vortex than the positive. Substantially similar results were obtained when employing the maximum vorticity magnitude of each vortex as opposed to the circulation Γ_x.

Conclusions

Stereoscopic particle image velocimetry data have been collected for a supersonic jet exhausting from a laterally inclined nozzle into a transonic crossflow. The nozzle inclination produces an exit plane scarfed by the flat plate in which it is installed, such that the expansion length of the nozzle varies across its exit plane to yield a range of exit Mach numbers. Measurements were conducted exclusively in the crossplane of the interaction 33.8 jet diameters downstream of the jet nozzle centerline. Mean velocity fields were found for a set of flow conditions in which the jet-to-freestream dynamic pressure ratio J, determined at the nozzle centerline, was varied at a constant freestream Mach number of 0.8 for nozzle inclination angles of 0, 15, 30, and 45 deg. Vorticity fields were computed from the in-plane components of the velocity data.

The resulting velocity and vorticity fields distinctly show the strength and location of the induced counterrotating vortex pair as well as the remnant of the horseshoe vortex that wraps around the jet plume as it first exhausts from the nozzle. For the normal nozzle (i.e., no nozzle cant), the vortex structure is symmetric to within the experimental uncertainty and the size and strength of the counterrotating vortex pair increase for larger values of J while it moves further from the wall. As the nozzle inclination is raised to 15 deg, the vortex pair becomes tilted opposite the direction of the nozzle cant and the vortex nearer to the wall generally attains a larger strength than its counterpart. Both trends become even stronger at a nozzle cant of 30 deg, and at a cant angle of 45 deg, the vortex near the wall becomes so dominant that the opposite vortex frequently is undetectable. Simultaneous with these trends, the vortices shift closer to the wall for larger nozzle inclination and become increasingly laterally displaced from the nozzle exit. Regardless of the nozzle cant, the vortex strengths increase with larger J. At lower nozzle cants, the distance of the vortices from the wall increases with J; however, as the nozzle inclination is increased, the position of the vortex nearer to the wall shows less variation with J than does its complement. Assembling these observations, this means that at a sufficiently large cant angle, the vortex structure produced by the jet interaction is effectively a single vortex whose position does not shift greatly as the jet strength is increased.

The vortex positions and their associated strengths that have been determined herein provide guidance toward the prediction of jet/fin interaction effects by offering a measure of the flowfield that can be expected to impinge upon downstream control surfaces on a flight vehicle. The scarfed nozzle geometry employed in the present jet-in-crossflow investigation examines rocket nozzle designs realistic to application for attitude or roll control on an atmospheric flight body, and hence offers a higher level of fidelity as compared with the more commonly studied symmetric configuration.

Acknowledgments

This work is supported by Sandia National Laboratories and the United States Department of Energy. Sandia is a multiprogram laboratory operated by Sandia Corporation, a Lockheed Martin Company, for the United States Department of Energy's National Nuclear Security Administration under Contract DE-AC04-94AL85000. The authors would like to thank W. L. Oberkampf, C. W. Peterson, and W. P. Wolfe, all of Sandia National Laboratories, for their helpful suggestions regarding this work.

References

[1] Cassel, L. A., Durando, N. A., Bullard, C. W., and Kelso, J. M., "Jet Interaction Control Effectiveness for Subsonic and Supersonic Flight," Rept. No. RD-TR-69-21, U.S. Army Missile Command, Redstone Arsenal, Sept. 1969.

[2] Dormieux, M., and Marsaa-Poey, R., "Numerical Assessment of Aerodynamic Interactions on Missiles with Transverse Jets Control," *Computational and Experimental Assessment of Jets in Cross Flow*, AGARD CP 534, 1993, pp. 30.1–30.11.

[3] Cassel, L. A., "Applying Jet Interaction Technology," *Journal of Spacecraft and Rockets*, Vol. 40, No. 4, 2003, pp. 523–537.

[4] Srivastava, B., "Aerodynamic Performance of Supersonic Missile Body- and Wing Tip-Mounted Lateral Jets," *Journal of Spacecraft and Rockets*, Vol. 35, No. 3, 1998, pp. 278–286.

[5] Brandeis, J., and Gill, J., "Experimental Investigation of Super- and Hypersonic Jet Interaction on Missile Configurations," *Journal of Spacecraft and Rockets*, Vol. 35, No. 3, 1998, pp. 296–302.

[6] Graham, M. J., Weinacht, P., and Brandeis, J., "Numerical Investigation of Supersonic Jet Interaction for Finned Bodies," *Journal of Spacecraft and Rockets*, Vol. 39, No. 3, 2002, pp. 376–383.

[7] Margason, R. J., "Fifty Years of Jet in Cross Flow Research," *Computational and Experimental Assessment of Jets in Cross Flow*, AGARD CP 534, 1993, pp. 1.1–1.41.

[8] Fric, T. F., and Roshko, A., "Vortical Structure in the Wake of a Transverse Jet," *Journal of Fluid Mechanics*, Vol. 279, 1994, pp. 1–47.

[9] Kelso, R. M., Lim, T. T., and Perry, A. E., "Experimental Study of Round Jets in Crossflow," *Journal of Fluid Mechanics*, Vol. 306, 1996, pp. 111–144.

[10] McCann, G. J., and Bowersox, R. D. W., "Experimental Investigation of Supersonic Gaseous Injection into a Supersonic Freestream," *AIAA Journal*, Vol. 34, No. 2, 1996, pp. 317–323.

[11] Santiago, J. G., and Dutton, J. C., "Velocity Measurements of a Jet Injected into a Supersonic Crossflow," *Journal of Propulsion and Power*, Vol. 13, No. 2, 1997, pp. 264–273.

[12] Krothapalli, A., Lourenco, L., and Buchlin, J. M., "Separated Flow Upstream of a Jet in a Crossflow," *AIAA Journal*, Vol. 28, No. 3, 1990, pp. 414–420.

[13] Kelso, R. M., and Smits, A. J., "Horseshoe Vortex Systems Resulting from the Interaction between a Laminar Boundary Layer and a Transverse Jet," *Physics of Fluids*, Vol. 7, No. 1, 1995, pp. 153–158.

[14] Beresh, S. J., Henfling, J. F., Erven, R. J., and Spillers, R. W., "Penetration of a Transverse Supersonic Jet into a Subsonic Compressible Crossflow," *AIAA Journal*, Vol. 43, No. 2, 2005, pp. 379–389.

[15] Beresh, S. J., Henfling, J. F., Erven, R. J., and Spillers, R. W., "Turbulent Characteristics of a Transverse Supersonic Jet in a Subsonic Compressible Crossflow," *AIAA Journal*, Vol. 43, No. 11, 2005, pp. 2385–2394.

[16] Beresh, S. J., Henfling, J. F., Erven, R. J., and Spillers, R. W., "Crossplane Velocimetry of a Transverse Supersonic Jet in a Transonic Crossflow," AIAA Paper 2006-0906, Jan. 2006;also *AIAA Journal* (to be published).

[17] Krausche, D., Fearn, R. L., and Weston, R. P., "Round Jet in a Cross Flow: Influence of Injection Angle on Vortex Properties," *AIAA Journal*, Vol. 16, No. 6, 1978, pp. 636–637.

[18] Compton, D. A., and Johnston, J. P., "Streamwise Vortex Production by Pitched and Skewed Jets in a Turbulent Boundary Layer," *AIAA Journal*, Vol. 30, No. 3, 1992, pp. 640–647.

[19] Zhang, X., and Collins, M. W., "Nearfield Evolution of a Longitudinal Vortex Generated by an Inclined Jet in a Turbulent Boundary Layer," *Journal of Fluids Engineering*, Vol. 119, No. 4, 1997, pp. 934–939.

[20] Khan, Z. U., and Johnston, J. P., "Vortex Generating Jets," *International Journal of Heat and Fluid Flow*, Vol. 21, No. 5, 2000, pp. 506–511.

[21] Han, D., Orozco, V., and Mungal, M. G., "Gross-Entrainment Behavior of Turbulent Jets Injected Obliquely into a Uniform Crossflow," *AIAA Journal*, Vol. 38, No. 9, 2000, pp. 1643–1649.

[22] Milanovic, I. M., and Zaman, K. B. M., "Fluid Dynamics of Highly Pitched and Yawed Jets in Crossflow," *AIAA Journal*, Vol. 42, No. 5, 2004, pp. 874–882.

[23] Gruber, M. R., Nejad, A. S., Chen, T. H., and Dutton, J. C., "Mixing and Penetration Studies of Sonic Jets in a Mach 2 Freestream," *Journal of Propulsion and Power*, Vol. 11, No. 2, 1995, pp. 315–323.

[24] Bowersox, R. D. W., Fan, H., and Lee, D., "Sonic Injection into a Mach 5.0 Freestream Through Diamond Orifices," *Journal of Propulsion and Power*, Vol. 20, No. 2, 2004, pp. 280–287.

[25] Fuller, E. J., Mays, R. B., Thomas, R. H., and Schetz, J. A., "Mixing Studies of Helium in Air at High Supersonic Speeds," *AIAA Journal*, Vol. 30, No. 9, 1992, pp. 2234–2243.

[26] Bowersox, R. D. W., "Turbulent Flow Structure Characterization of Angled Injection into a Supersonic Crossflow," *Journal of Spacecraft and Rockets*, Vol. 34, No. 2, 1997, pp. 205–213.

[27] Lilley, J. S., and Hoffman, J. D., "Performance Analysis of Scarfed Nozzles," *Journal of Spacecraft and Rockets*, Vol. 23, No. 1, 1986, pp. 55–62.

[28] Beresh, S. J., Henfling, J. F., and Erven, R. J., "Flow Separation Inside a Supersonic Nozzle Exhausting into a Subsonic Compressible Crossflow," *Journal of Propulsion and Power*, Vol. 19, No. 4, 2003, pp. 655–662.

[29] Samimy, M., and Lele, S. K., "Motion of Particles with Inertia in a Compressible Free Shear Layer," *Physics of Fluids A*, Vol. 3, No. 8, 1991, pp. 1915–1923.

[30] Melling, A., "Tracer Particles and Seeding for Particle Image Velocimetry," *Measurement Science and Technology*, Vol. 8, No. 12, 1997, pp. 1406–1416.

[31] Soloff, S. M., Adrian, R. J., and Liu, Z.-C., "Distortion Compensation for Generalized Stereoscopic Particle Image Velocimetry," *Measurement Science and Technology*, Vol. 8, No. 12, 1997, pp. 1441–1454.

[32] Luff, J. D., Drouilliard, T., Rompage, A. M., Linne, M. A., and Hertzberg, J. R., "Experimental Uncertainties Associated with Particle Image Velocimetry (PIV) Based Vorticity Algorithms," *Experiments in Fluids*, Vol. 26, Nos. 1–2, 1999, pp. 36–54.

[33] Sykes, R. I., Lewellen, W. S., and Parker, S. F., "On the Vorticity Dynamics of a Turbulent Jet in a Crossflow," *Journal of Fluid Mechanics*, Vol. 168, 1986, pp. 393–413.

[34] Haven, B. A., and Kurosaka, M., "Kidney and Anti-Kidney Vortices in Crossflow Jets," *Journal of Fluid Mechanics*, Vol. 352, 1997, pp. 27–64.

[35] Yuan, L. L., Street, R. L., and Ferziger, J. H., "Large-Eddy Simulations of a Round Jet in Crossflow," *Journal of Fluid Mechanics*, Vol. 379, 1999, pp. 71–104.

[36] Lim, T. T., New, T. H., and Luo, S. C., "On the Development of Large-Scale Structures of a Jet Normal to a Cross Flow," *Physics of Fluids*, Vol. 13, No. 3, 2001, pp. 770–775.

[37] Beresh, S. J., Heineck, J. T., Walker, S. M., Schairer, E. T., and Yaste, D. M., "Stereoscopic PIV for Jet/Fin Interaction Measurements on a Full-Scale Flight Vehicle Configuration," AIAA Paper 2005-0442, Jan. 2005.

R. Bowersox
Associate Editor